Journal of Molecular Modeling (2022) 28: 65
https://doi.org/10.1007/s00894-022-05047-5

ORIGINAL PAPER

Growth, crystal structure, Hirshfeld surface analysis, DFT studies, physicochemical characterization, and cytotoxicity assays of novel organic triphosphate

Yathreb Oueslati[1] · Sevgi Kansız[2] · Necmi Dege[3] · Cristina de la Torre Paredes[4] · Antoni Llopis-Lorente[4] · Ramón Martínez-Máñez[4] · Wajda Smirani Sta[1]

Received: 17 July 2021 / Accepted: 4 February 2022 / Published online: 19 February 2022

Abstract
A novel organic–inorganic hybrid compound, named (1-phenylpiperazinium) trihydrogen triphosphate, with the formula $(C_{10}H_{15}N_2)_2H_3P_3O_{10}$ has been obtained by low speed of evaporation of a mixture of an alcoholic solution of 1-phenylpiperazine and triphosphoric acid $H_5P_3O_{10}$ at room temperature after using the ion exchange chemical procedure. To carry out a detailed crystallographic structure analysis, single-crystal X-ray diffraction has been reported. In the molecular arrangement, the different entities are held together through N–H···O, O–H···O, and C-H···O hydrogen bonds, building up a three-dimensional packing. Powder X-ray diffraction analysis is acquired to confirm the purity of the product. The nature and the proportion of intermolecular interactions were investigated by Hirshfeld surface analysis. In order to support the experimental results, a density functional theory (DFT) calculation was performed, using the Becke-3-parameter-Lee–Yang–Parr (B3LYP) function with LANL2DZ basis set, and the data indicate much agreement between the experimental and the theoretical results. Thus, the physicochemical properties were studied employing a variety of techniques (FTIR, NMR, UV–visible, and photoluminescence). To get an insight of the possible employment of the present material in biology, cell viability assays were performed.

Keywords Triphosphate · X-ray diffraction · Density functional theory · Hirshfeld surface · Spectroscopy · Cytotoxicity assays

Introduction

The scientific community has been focused more than ever in improvement and development of organic–inorganic hybrid materials due to the growing need for new sophisticated products to allow the access to various spectra of functionalities [1–7]. These composites become trend owing to their interesting features to gather the excellent merits of both organic and inorganic worlds on the molecular level. Up to date, hybrid solids are subject to many scientific studies due to their low cost, ease of synthesis, structural tenability, and specific physical, chemical, and biological properties. Such materials can be applied in both academic research and technological applications such as optic [8, 9], electronic [10], mechanics, sensors, magnetism [11, 12], catalysis, and medicine [13, 14].

In this context, the main focus was on the hybrid compounds based on phosphates, in particular. Among them, the choice was on the triphosphates, those with the formula of the anion $[P_3O_{10}]^{5-}$. Unsurprisingly, the number of these series of compounds remains limited in comparison with other condensed phosphates because they are chemically unstable in their synthesis. Indeed, the phosphoric chain containing three PO_4 tetrahedra, which are linked together by two internal oxygen atoms, can be destructed and gives either a diphosphate

✉ Wajda Smirani Sta
wajda_sta@yahoo.fr

1 Department of Chemistry, Faculty of Sciences of Bizerte, Carthage University, 7021 Zarzouna, Tunisia

2 Department of Fundamental Sciences, Faculty of Engineering, Samsun University, 55420 Samsun, Turkey

3 Department of Physics, Faculty of Arts and Sciences, Ondokuz Mayıs University, 55139 Samsun, Turkey

4 Department of Chemistry, Institute for Molecular Recognition and Technological Development (IDM), Polytechnic University of Valencia, Camino de Vera s/n, 46022 Valencia, Spain

or monophosphate compound. Since their first synthesis, only eight composites have appeared in literature. These include $(2\text{-}C_2H_5C_6H_4NH_3)_3H_2P_3O_{10}$ [15], $(C_4N_2H_{12})_2HP_3O_{10}.H_2O$ [16], $[(CH_3O)_2(C_6H_3NH_3)]_3H_2P_3O_{10}$ [17], $[4\text{-}(OCH_3)C_6H_4CH_2NH_3]_4H_2P_3O_{10}H_4P_3O_{10}$ [18], $[2,6\text{-}(C_2H_5)_2C_6H_3NH_3]_2H_3P_3O_{10}$ [19], $[2,3\text{-}(CH_3)_2C_6H_3NH_3]_4HP_3O_{10}.2H_2O$ [20], $[C_{12}H_{19}N_2]_3[H_2P_3O_{10}]0.3H_2O$ [21], and $(C_{12}H_{14}N_2O)_2HP_3O_{10}.2H_2O$ [22].

As for the organic materials, the aromatic amines have been widely acted as templates, termed structure directing agents, because of their important characteristics thanks to the presence of delocalized π-electrons. Piperazine derivatives present an important group of aromatic amines, which are composed of a six-member ring containing the two opposing nitrogen. These latter have been used as organic part in various compounds and are able to form a dication in the boat and chair forms. Owing to their excellent biological, pharmacology, and cardiovascular properties, piperazine derivatives are of great significance to the rational design of well-known drugs with various therapeutic uses, such as antimalarial agents [23, 24], anti-bacterial agents [25], anti-psychotic agents [26–28], anti-hypertension, antifungal [29], anti-inflammation [30], and cytotoxic. Due to the extensive use of these amines in wide variety of medical formulations, researcher efforts have focused in the synthesis of new materials consisting of piperazine derivates to expand their scope of application.

Within this context, we report in this work the synthesis of a novel triphosphate compound, named (1-phenylpiperazinium) trihydrogen triphosphate $(C_{10}H_{15}N_2)_2H_3P_3O_{10}$, through the method of crystallization. In order to reach a fine description of the architecture of the title compound and provide detailed information about the internal lattice of the crystal, a single-crystal X-ray diffraction was used. The optimized geometry was calculated using a method based on the density functional theory (DFT) employing B3LYP/LANL2DZ basis sets. Experimental data and theoretical calculations are compared. Furthermore, Hirshfeld surface analysis is required to elucidate the role of intermolecular contacts. A vibrational study was investigated and discussed. Frontier orbitals, Mulliken charges, and molecular electrostatic potential of the title compound have been calculated. The optical properties have been also well discussed in detail. Additionally, cell viability studies in the presence of the compound were also conducted in order to assess its biocompatibility and lack of cytotoxicity.

Materials and methods

Synthesis

Single crystals of $(C_{10}H_{15}N_2)_2H_3P_3O_{10}$ were obtained via an acid–base reaction under normal conditions of temperature and pressure. The chemical synthesis of the title compound was carried out in two steps: The triphosphoric acid was first prepared by passing a sodium salt solution of $Na_5P_3O_{10}$ (a starting material to prepare the organic triphosphates) through an ion exchange resin (Amberlite IR 120), and then an alcoholic solution of 1-phenylpiperazine was added drop by drop to this aqueous solution until a pH = 2.

Schematically the synthesis reaction is:

$$2\left(C_{10}H_{14}N_2\right) + H_5P_3O_{10} \rightarrow \left(C_{10}H_{15}N_2\right)H_3P_3O_{10}$$

After a few days of slow evaporation at 298 K, colorless transparent crystals appeared in the solution.

X-ray crystallography

The powder X-ray diffraction (PXRD) was performed using Cu-Kα ($\lambda = 1.5406$ Å) radiation on a Bruker D8-advance diffractometer; for typical powder patterns, data is collected at 2θ over the range of 0–40°. A tiny single crystal of approximate dimension $0.21 \times 0.16 \times 0.14$ mm^3 was chosen for the diffraction measurement. The data were collected at 293(2) K with an Enraf–Nonius MACH3 four-circle diffractometer, using graphite monochromated Mo-K_α radiation ($\lambda = 0.71073$ Å). The structure was solved and refined with SHELXT [31] and refined using SHELXL [32]. The drawing of the molecular structure was made with DIAMOND [33]. Further details of the structure analysis are reported in Table S1. The hydrogen bonds are given in Table S2. Hirshfeld surface and their associated two-dimensional fingerprint were plotted with the Crystal Explorer (version 3.1) software [34] which use the CIF files of the desired compound in order to analyze the intermolecular interactions in the crystal.

Computational methods

Gaussian03 program [35] was used for the quantum chemical calculations and the optimized molecular geometries. All the calculation results were visualized with the Gauss-View 4.1 [36]. The structure based on the crystallographic data in the supplementary table was used as starting points at the density functional theory (DFT) with the Becke-three-parameter hybrid exchange functional combined with the Lee–Yang–Parr correlation functional (B3LYP) levels. It is to be noted that the LANL2DZ was used as the basis set. The molecular electrostatic potential (MEP) map, Mulliken population charge, and FTIR spectrum of optimized structure were calculated at the same basis set. The calculated vibration frequencies were scaled using the scaling factor 0.9614 [37]. The absence of imaginary frequencies in the calculated vibrational spectrum confirms that the structure corresponds to minimum energy.

Spectroscopic measurements

A Nicolet IR200 FTIR equipped with a diamond micro-ATR was used to characterize the infrared stretching and bending bands of the (1-phenylpiperazinium) trihydrogen triphosphate in the 4000–400 cm^{-1} range.

Solid state UV–vis absorption spectra were performed on a Perkin Elmer Lambda 35 spectrophotometer in the range of 200–800 nm.

Emission spectrum was performed using the PerkinElmer LS55 fluorescence spectrometer equipped with a 450-W xenon lamp as the excitation source using solid sample at room temperature.

All NMR experiments were carried out using D_2O as solvent on a Bruker Avance III spectrometer operating at 400 MHz.

Biological assays

After in vitro characterization, the new organic triphosphate synthesized was evaluated in experiments with cells. These additional studies were undertaken to assess and to exclude any toxic effect of the compound. For these experiments, RAW 264.7 murine macrophage cell lines were used as model system. The cells were routinely grown in a DMEM (Dulbecco's modified Eagle's medium)/nutrient mixture F-12 ham containing 10% fetal calf serum (FCS) and 1% penicillin/streptomycin purchased from Sigma-Aldrich. The maintenance of the cell culture was carried out according to standard protocols provided by the European Collection of Authenticated Cell Cultures (ECACC). To study the effect of the synthesized compound, cells were seeded in 24-well culture plates at a density of 1.510^6 cells per well and treated with the corresponding concentration of compound (ranging from 100 µM to 10 nM) for 24 h. Then, the medium was gently aspirated and cells were washed with PBS. Then, 200 µL of a solution of an MTT (0.1 mg mL^{-1}) in fresh medium was added and the cells were incubated for 45 min at 37 °C. Finally, the medium was aspirated and 200 µL of DMSO was added to measure absorbance of each well at 492 nm using a 96-well multiwell plate reader (Wallac 1420 VICTOR2TM, Perkin Elmer). Three independent experiments were carried out.

Results and discussion

Description of the crystal structure

X-ray diffraction patterns of the experimental and the simulated studied sample are shown in Fig. 1. Both the peak positions displayed in the measured patterns and the simulated patterns are in good line. This result reveals clearly that the synthesis product is in pure phase. A slight difference in the positions and intensities of some peaks can be observed, which are ascribed to the preferred orientation of the powder samples. It is noted that some of the extra unexpected lines with weak intensities are observed which is certainly due to the presence of some impurities in the powder sample that are absent in the single-crystal state.

An ORTEP plot of $(C_{10}H_{15}N_2)_2H_3P_3O_{10}$ is shown in Fig. S1. This structural model in which the asymmetric unit contains one inorganic anion $[H_3P_3O_{10}]^{2-}$ and two organic cations denoted $[C_{10}H_{15}N_2]^+$ crystallographically independent.

Figure 2 displays the projection of the structure of (1-phenylpiperazinium) trihydrogen triphosphate in the (ac) plane. Indeed the examination of the latter manifests the existence of infinite layers of anions $[H_3P_3O_{10}]^{2-}$ located at $z=0$ between them, and the organic cations are inserted giving rise to a three-dimensional network through N–H···O and C-H···O hydrogen bonds. Inside such a layer, two $H_3P_3O_{10}{}^{2-}$ anions are linked together via strong O(1)-H(8)···O(10) hydrogen bond to form $H_6P_6O_{20}{}^{4-}$ cyclic units (Fig. S2(a)) which are interconnected by strong hydrogen bond interactions [O(9)···O(8): 2.624(4)Å, O(1)···O(10): 2.557(4)Å] to develop a layer parallel to (a, b) plane. These associations created an $R_2^2(16)$ ring graph set as shown in Fig. S2(b).

The $P_3O_{10}{}^{5-}$ is formed by three independent tetrahedra PO_4 groups which are bonded via two bridge oxygen O4 and O5. $[H_2PO_3-O-PO_2-O-HPO_3]$ is the detailed geometry of the triphosphate group. Table 1 depicts the PO_4 distances inside the $H_3P_3O_{10}{}^{2-}$ anion, as usually observed for all condensed phosphates, and there are

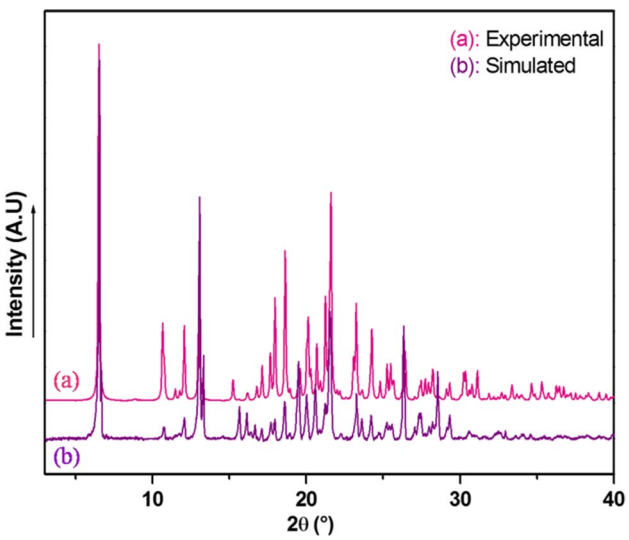

Fig. 1 Experimental and simulated powder XRD patterns of the prepared compound $(C_{10}H_{15}N_2)_2H_3P_3O_{10}$

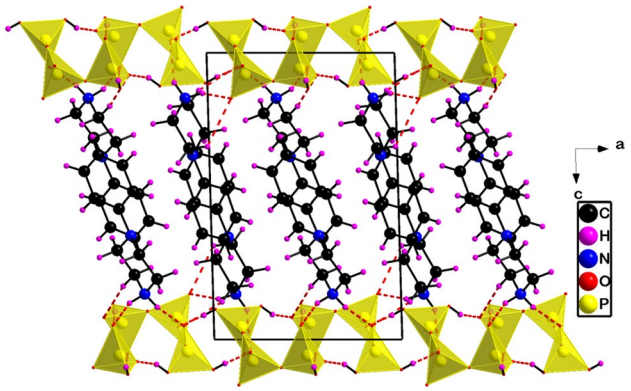

Fig. 2 Projection of the crystal structure of $(C_{10}H_{15}N_2)_2H_3P_3O_{10}$ in the (ac) plane

Table 1 Main interatomic distances (Å) and bond angles (°) of $H_3P_3O_{10}^{2-}$

P(1)	**O(7)**	**O(5)**	**O(6)**	**O(4)**
O(7)	*1.3190 (15)*	101.30 (10)	112.17 (12)	113.91 (11)
O(5)	2.1886 (21)	*1.5070 (16)*	117.54 (10)	98.52 (10)
O(6)	2.4264 (28)	2.6564 (24)	*1.5991 (19)*	112.39 (9)
O(4)	2.6146 (25)	2.5011 (25)	2.814 (3)	*1.7852 (5)*
P(2)	**O(3)**	**O(1)**	**O(2)**	**O(4)**
O(3)	*1.4258 (18)*	110.01 (12)	121.26 (12)	109.60 (11)
O(1)	2.3561 (27)	*1.450 (2)*	95.94 (13)	115.88 (13)
O(2)	2.5519 (26)	2.1854 (24)	*1.5019 (19)*	104.35 (11)
O(4)	2.6618 (29)	2.7781 (28)	2.6308 (32)	*1.820 (2)*
P(3)	**O(5)**	**O(8)**	**O(10)**	**O(9)**
O(5)	*1.3786 (15)*	105.77 (10)	101.72 (12)	100.91 (12)
O(8)	2.2818 (24)	*1.4822 (18)*	113.89 (14)	113.82 (11)
O(10)	2.2831 (22)	2.5508 (28)	*1.561 (2)*	118.06 (16)
O(9)	2.4308 (40)	2.7191 (33)	2.8476 (39)	*1.758 (3)*
P(2)-P(1) = 3.357 (10)		P(1)-O(4)-P(2) = 137.31 (10)		
P(1)-P(3) = 2.604 (10)		P(1)-O(5)-P(3) = 128.87 (12)		
P(2)-O(1)-H(8) = 110.06 (3)		O(1)-H(8) = 0.99 (6)		
		O(2)-H(9) = 0.89 (4)		
P(2)-O(2)-H(9) = 102.60 (3)		O(9)-H(7) = 0.75 (5)		
P(3)-O(9)-H(7) = 118.33 (4)				

The italicized values indicate the P-O distances

different types of PO distances inside the PO_4 tetrahedron. The longest ones with average value equal to 1.6227 Å correspond to the two bridging oxygen atoms, the intermediate ones with average value equal to 1.569 Å correspond to the P-OH bonding, and the shortest ones with average value equal to 1.477 Å correspond to the external oxygen atoms. The average values for the P-O distances and O–P–O angles are 1.548 Å and 109.36°, and the O–P–O average angle is always very close to 109°. Such distances and angles are quite similar to those measured in other triphosphate anions [15].

The average values of the distortion indices were calculated using the Baur method [38] which is based on the following formula:

$$\mathrm{ID(PO)} = \frac{\sum_i |PO_i - PO_m|}{\sum_i PO_i},\ \mathrm{ID(OO)} = \frac{\sum_i |OO_i - OO_m|}{\sum_i OO_i} \text{ and } \mathrm{ID(OPO)} = \frac{\sum_i |OPO_i - OPO_m|}{\sum_i OPO_i}$$

The results of the calculation are [DI (OPO) = 0.057; DI (PO) = 0.083; and DI (OO) = 0.068]. Reviewing these values we can conclude that the distortion in the P-O distances is slightly higher than O–O distances. In this structure, the PO_4 group can be regarded as a regular arrangement of oxygen atoms with the phosphorus atom softly displaced from the gravity center. The two crystallographically independent organic cations adopt a chair conformation, which is the most stable conformation. The conformation of the piperazine six-membered ring can be described in terms of Cremer and Pople puckering coordinates [39]. In this crystal structure, the puckering parameters are as follows: QT = 0.5174 Å, q2 = 0.0123 Å, q3 = 0.5172 Å, θ = 1.36°, and ϕ = −61.79° for the (N2-C10-C9-N1-C7-C8) ring and QT = 0.5432 Å, q2 = 0.0432 Å, q3 = 0.5415 Å, θ = 4.56°, and ϕ = 176.67° for the (N4-C19-C18-N3-C17-C20) ring. DFT calculations were applied on $(C_{10}H_{15}N_2)_2H_3P_3O_{10}$ at B3LYP/LANL2DZ level. The optimized structure of the title compound is illustrated in Fig. 3.

The experimental and theoretical structural parameters of the studied compound are given in Table 2. After a careful comparison, we find that the optimized parameters such as bond lengths, bond angles, and torsion angles are compatible with those determined using single-crystal X-ray diffraction method. The slight minor deviations observed can be explained by the fact that the experimental data is obtained in the solid state in the gaseous phase, whereas in the theoretical methods the molecular interactions are not taken into account. As shown, the optimized parameters (bond lengths, bond angles) are very close with the experimental data (Fig. S3). The calculated geometrical parameters of the anionic entity $H_3P_3O_{10}$ go in good consistency with those found in other studies especially with methyl triphosphate (− 1) that are predicted by DFT/6-31G* method of computations [40].

Hirshfeld surface studies

Surface analysis is a powerful tool in the visualization and exploration of the intermolecular interactions in the crystal structure of compound. The Crystal Explorer 3.1 program which processes structure input files in the CIF format was used to calculate Hirshfeld surfaces [41] and their associated two-dimensional fingerprint plots (2D fingerprint) [42] which summarize and provide relevant information of all the intermolecular interactions in the crystal. The normalized

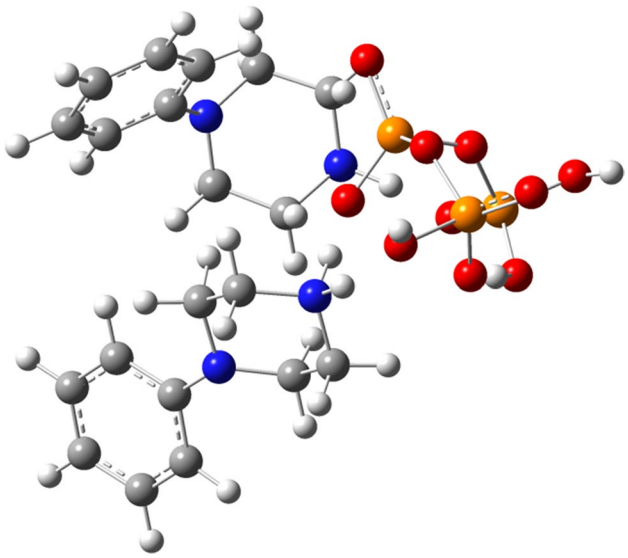

Fig. 3 The optimized geometric structure of $(C_{10}H_{15}N_2)_2H_3P_3O_{10}$

Table 2 Some selected geometric parameters for $(C_{10}H_{15}N_2)_2H_3P_3O_{10}$ (Å, °)

Geometric parameters	Experimental (X-ray diffraction)	Calculated DFT
Bond lengths (Å)		
P1—O4	1.785 (2)	1.706
P1—O5	1.506 (2)	1.579
P1—O6	1.598 (2)	1.658
P2—O1	1.450 (2)	1.556
P2—O2	1.500 (2)	1.646
P2—O3	1.425 (2)	1.568
P3—O8	1.481 (2)	1.627
N1—C1	1.435 (3)	1.443
N1—C7	1.550 (4)	1.474
N2—C8	1.610 (4)	1.518
N2—C10	1.576 (4)	1.508
N3—C11	1.416 (3)	1.428
N3—C18	1.336 (3)	1.456
N4—C19	1.671 (4)	1.513
Bond angles (°)		
O1—P2—O2	95.55 (15)	100.8
O4—P2—O1	115.89 (14)	112.68
O8—P3—O9	113.79 (11)	113.16
P1—O5—P3	128.85 (13)	134.98
C1—N1—C7	116.6 (2)	115.84
C11—N3—C18	115.7 (2)	110.50
C8—N2—C10	121.8 (2)	122.07
C19—N4—C20	115.0 (2)	112.19

contact distance (d_{norm}), based on two types of distances defined: d_e, the distance from the point to the nearest nucleus external to the surface, and d_i, the distance to the nearest nucleus internal to the surface, respectively is calculated via the following expression:

$$d_{norm} = \frac{d_i - r_i^{vdw}}{r_i^{vdw}} + \frac{d_e - r_e^{vdw}}{r_e^{vdw}}$$

where r_i^{vdw} is the van der Walls radius of the atom that lies inside the surface of Hirshfeld, while r_e^{vdw} is the van der Walls radius of the atom that lies outside of the surface of Hirshfeld.

For describing the surface characteristics of the crystal structure, Hirshfeld surface and two-dimensional fingerprint plots are useful tools using the *Crystal Explorer* package. Hirshfeld surface of $(C_{10}H_{15}N_2)_2H_3P_3O_{10}$ with mapped d_{norm} is portrayed in Fig. 4.

The surface of the three-dimensional d_{norm} was obtained in the range − 0.830 (red) to 1.414 (blue) using a standard (high) surface resolution for the title compound. A red-white-blue color scheme is used for the analysis of the molecular. The inter-contacts included in hydrogen bonds are represented with the red spots over Hirshfeld surface. The blue fields indicate areas where neighboring atoms are too far away to interact with each other [43–47] and the white color is used for the contacts around the sum of van der Waals radii (vdW). The red regions are apparent above the oxygen atoms participating in the C-H···O, N–H···O, and O–H···O contacts.

The overall fingerprint plot for the studied compound is shown in Fig. 5a; the examination of decomposed 2D fingerprint plots shows that the O…H/H…O contacts represent the largest relative contribution, amounting to 43.7% in the compound, appearing as two symmetric long spikes (Fig. 5b). The value

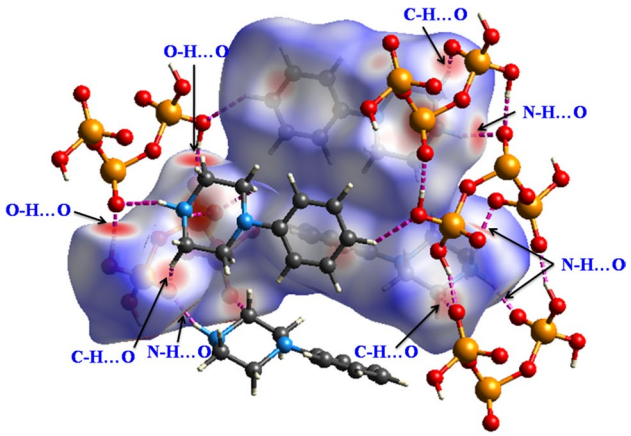

Fig. 4 Hirshfeld surface of $(C_{10}H_{15}N_2)_2H_3P_3O_{10}$ mapped on the d_{norm}

$(d_e + d_i) \sim 1.6$ Å is less than the sum of van der Waals radii of oxygen (1.52 Å) and hydrogen (1.20 Å) atoms. This result allows us to confirm that the inter-contact is considered being close contact. Furthermore, the H···H contacts constitute the second major frequent interactions in view of the abundance of hydrogen on the molecular surface with percentage contributions of 39.7% (Fig. 5c). These contacts appear as a single broad peak at $d_e = d_i \sim 1$ Å, and it should be also noted that $(d_e + d_i) \sim 2$ Å, which is longer than the generally accepted van der Waals radius for hydrogen atom. The C···H/H···C contacts cover 12.9% of the total surface and appear as two broad short spikes (Fig. 5d). The H···N/N···H and O···O contacts comprise 2.1% and 1% respectively. These contacts have very little effect on crystal packing (Fig. 5e, f). C···C and P···O/O···P contacts are the less contributed to the Hirshfeld surfaces with a small percentage of 0.3% and 0.2% on the Hirshfeld surface, respectively (Fig. 5g, h).

2D fingerprint (full and decomposed) plot with combination of d_e and d_i provides summary of intermolecular contacts in the crystal. The breakdown of FP into specific atom…atom contacts in a crystal provides the types of intermolecular contacts experienced by the molecule quantitatively.

Thus, fingerprint graphics and the molecular Hirshfeld surface are a good way to understand the contributions of diverse contacts that assist stabilize molecular structures.

IR spectroscopy

The IR spectroscopy has been used due to its usefulness in the determination and the identification of the frequencies of the vibrations on the crystal structure. The theoretical IR spectrum, calculated by using DFT/B3LYP method with LANL2DZ basis set, was made on the optimized geometries of the compound. The scaling factor is taken as 0.9614 to reduce the discrepancy between the experimental frequencies and the computational methods. For visual comparison, the theoretical IR spectrum and the experimental one are schematically illustrated in Fig. 6. The detailed assignments of the scaled calculated and vibrational experimental modes are quoted in Table 3.

The bands appeared in the region of 1300 to 1100 cm^{-1}, which is an important region for the identification of the stretching vibrations, asymmetric symmetric, of the PO_2 central atomic group. The peaks detected between 1259 and 966 cm^{-1} are attributed to the stretching vibrations of the PO_3 terminal atomic groups [48]. These vibrations are well observed by DFT calculation in the range 1086 to 959 cm^{-1}. The stretching P-O-P modes are located in the 896 to 687 cm^{-1} region [49]. This mode was predicted by DFT calculation at 840 cm^{-1}. The bands which appear between 600 and 400 correspond to the bending vibrations of the PO_3 terminal groups while the DFT calculation gives these modes between 673 and 577 cm^{-1}.

The bands which are located in the high-frequency region, those between 3100 and 3000 cm^{-1}, are generally due to the

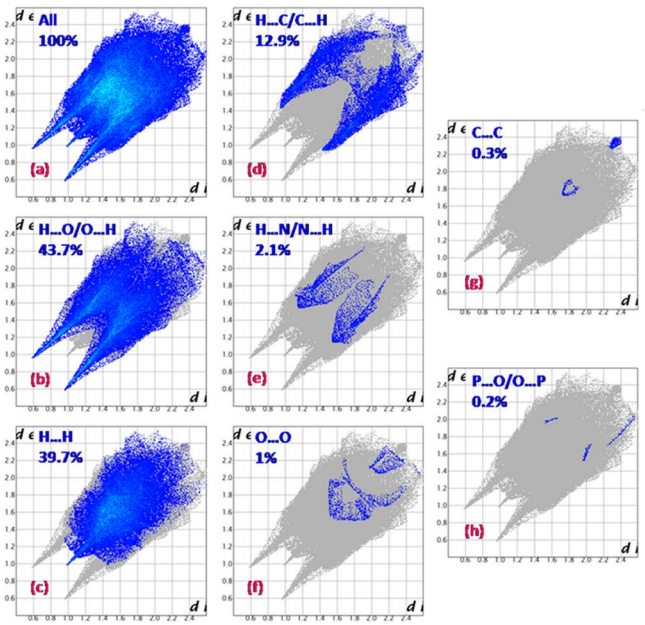

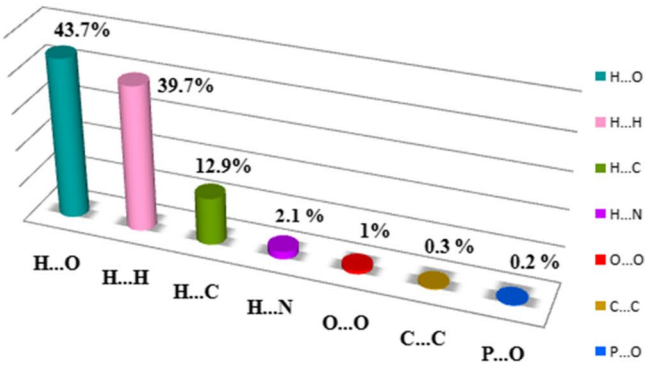

Fig. 5 Two-dimensional fingerprint plots showing the contributions of atoms within specific interacting pairs (blue areas). For each fingerprint map, the gray area is a representation of the whole plot. **a** All intermolecular contacts. **b** H···O/O···H (43.7%). **c** H···H (39.7%). **d** H···C/C···H (12.9%). **e** H…N/N…H (2.1%). **f** O…O (1%). **g** C…C (0.3%). **h** P…O/O…P contacts in $(C_{10}H_{15}N_2)_2H_3P_3O_{10}$

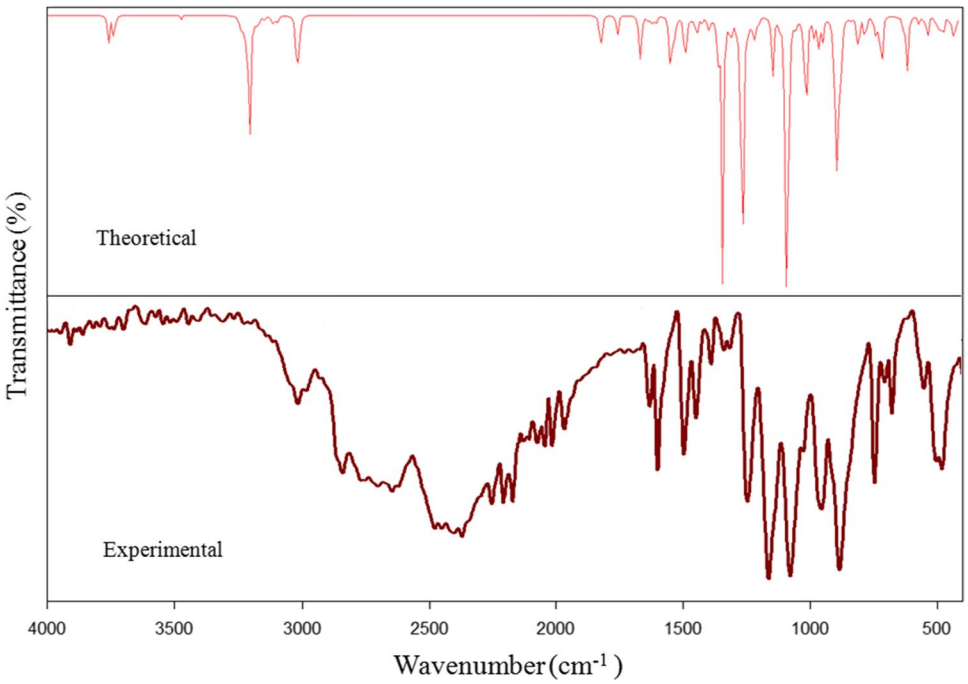

Fig. 6 Simulated IR spectra of $(C_{10}H_{15}N_2)_2H_3P_3O_{10}$ computed at B3LYP/LANL2DZ basis set (red). FTIR spectrum (blue)

Table 3 Comparison of the observed and calculated vibrational mode frequencies

Assignments	Experimental IR (cm^{-1})	Calculated B3LYP/LANL2DZ
$\nu_{asym}(NH_2)$	-	3326
$\nu_{sym}(NH_2)+\nu_{ar}$ (CH)	3100 to 3000	3070
$\nu_{sym}(CH_2)$	3000 to 2800	2894
$\beta_{in\ plane}(NH_2)$	-	1738
ν(C=C)	1644 to 1325	1590
$\beta_{in\ plane,\ ar}$ (CH)	-	1475
β(OH)	-	1418, 1273, 1201
$\nu(PO_3)$	1259 to 966	1086, 1034, 959
ν(POP)	896 to 687	840
$\beta(PO_3)$	600 to 400	673, 577

asymmetric stretching vibration ν_{as}(C-H) of aromatic ring, while the symmetric stretching vibration ν_s(C-H) of the cyclic ring are displayed in the range of 2990 to 2900 cm^{-1}. It is clearly observed that the bands in 2836 to 2250 cm^{-1} correspond to the stretching vibrations of the $-NH_2^+$, $-CH_2$, and N–H group. The theoretical calculations have predicted the stretching $-NH_2$ and C-H mode at 3070 cm^{-1}. It is well known that the wavenumber of the C=C stretching vibration, known as semicircle stretching, is observed normally between 1600 and 1400 cm^{-1} [50, 51]. In this study, the peaks from 1644 to 1325 cm^{-1} are attributed to the symmetric and asymmetric stretching vibrations ν(C=C), the deformation modes δ(N–H), and ν(O–H) of P-OH groups. The theoretical calculations show that the bands corresponding to the ν(C=C) are detected at 1590 cm^{-1}. The bands between 1455 and 1333 cm^{-1} are assigned to $-CH_2$ deformation modes. The bands situated at 1260 and 1168 cm^{-1} are due to (C-N) stretching. The peak at 1089 cm^{-1} is assigned to asymmetric and symmetric C–C stretching modes. Bands detected between 965 and 902 cm^{-1} are attributed to (C-H) out-of-plane deformation. Bands which appear between 764 and 691 cm^{-1} are assigned to (C-N) and (C–C) out-of-plane deformation. Finally, those observed at 569 to 496 cm^{-1} are attributed to the mode of deformation of the group δ (C=C) out of the plane. It is obvious that the theoretical IR spectrum shows a good conformity with the experimental one (Fig. S4).

Frontier molecular orbital analysis

The highest occupied molecular orbital (HOMO), which is the orbital that acts as an electron donor, the lowest unoccupied molecular orbital (LUMO), which is the orbital that acts as electron acceptor, and their electronic band gap are the most important parameters in the field of theoretical quantum chemistry for understanding the chemical reactivity of the molecules and their stability [52–54]. The electron distributions of the HOMO–LUMO energy for the synthesized compound computed at the Becke's three-parameter functional and the Lee–Yang–Parr functional (B3LYP) with the basis set LANL2DZ are depicted in Fig. 7.

The HOMO and LUMO energies, the energy gap, and other chemical reactivity descriptors that could be used to predict the chemical stability and reactivity, such as the ionization potential (*I*), the electron affinity (*A*), the

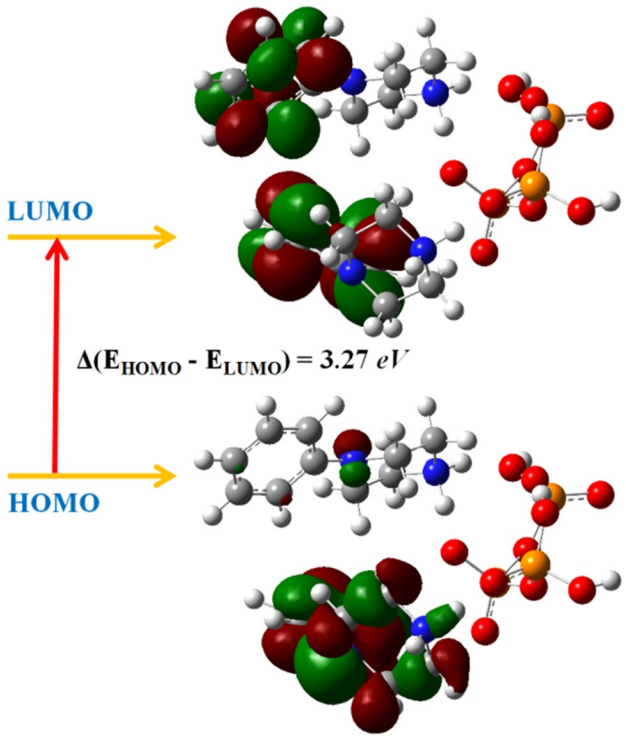

Fig. 7 The electron distribution of the HOMO and LUMO energy levels

Table 4 The calculated parameters of $(C_{10}H_{15}N_2)_2H_3P_3O_{10}$ using B3LYP/LANL2DZ level

Parameters		B3LYP/LAN-L2DZ
HOMO energy	E_{HOMO} (eV)	−8.21
LUMO energy	E_{LUMO} (eV)	−4.94
Energy gap	$\Delta E = E_{HOMO} - E_{LUMO}$ (eV)	−3.27
Iionization potential	$IP = -E_{HOMO}$ (eV)	8.21
Electron affinity	$EA = -E_{LUMO}$ (eV)	4.94
Electronegativity	$\chi = (IP + EA)/2$ (eV)	6.58
Hardness	$\eta = (IP - EA)/2$ (eV)	1.64
Softness	$\sigma = 1/\eta$ (eV)	0.30

electronegativity (χ), the softness (σ), and the hardness (η) for the $(C_{10}H_{15}N_2)_2H_3P_3O_{10}$ molecule, were also calculated at the same basis set and the results are reported in Table 4. For the title compound, the computed gas phase HOMO and LUMO energies are −8.21 eV and −4.94 eV respectively, whereas the energy gap is found 3.27 eV. This value obtained by DFT calculations is in good agreement with the optical band gaps calculated from the UV–vis absorption (2.82 eV). The slight difference is due to the calculations made in the gas phase, where interactions between molecules are not taken into account. Actually, in crystal structure, each group of the molecule is surrounded with other types of molecule groups via intermolecular interactions.

The large values of the electronic band gaps for $(C_{10}H_{15}N_2)_2H_3P_3O_{10}$ favor their hard nature with low chemical reactivity and high stability. The chemical hardness (η) calculated as $[-(E_{HOMO} - E_{LUMO})/2]$ is found 1.64 eV, and this value reflects that the compound is chemically stable. The softness (σ), which is the reciprocal of the hardness calculated as $[-2(E_{HOMO} - E_{LUMO})]$, is found 0.30 eV. The obtained small hardness parameters indicate that the title compound is a hard system which is not prone to chemical reaction and prove also that this compound presents high kinetic stability. The chemical reactivity descriptors used the following equations [55, 56]:

The electron affinity (EA) $EA = -E_{LUMO}$ (1)

The ionization potential (IP) $IP = -E_{HOMO}$ (2)

Absolute electronegativity (χ) and chemical potential (μ)

$$\chi = -\mu = \frac{(IP + EA)}{2} \quad (3)$$

Absolute hardness(η) $\eta = \frac{IP-EA}{2}$ (4)

Softness(σ) $\sigma = \frac{1}{\eta}$ (5)

Molecular electrostatic potential

The molecular electrostatic potential (MEP) is a powerful descriptor and an effective approach in understanding the intermolecular and intramolecular interactions in the solid states and offers quite accurate information about sites for electrophilic and nucleophilic. In other words, it is able to convey information about the interaction, active sites, and charge distribution of a molecule. Calculation of MEP was conducted at a high theoretical DFT level using B3LYP/LANL2DZ level of theory and is given in Fig. 8. As you can see in the three-dimensional model of the electrostatic potential map, a color spectrum ranging from red to dark blue, with red as the lowest electrostatic potential energy value indicating the nucleophilic region with rich electrons in the environment, blue-colored region as the highest, is employed to convey the varying intensities of the electrostatic potential energy values and the green color stands for the parts of the molecule where the electrostatic potentials are close to zero (neutral areas). The electrostatic potential increases in the order red < orange < yellow < green < blue. These sites provide information about the region in which the molecules can interact with each other and the hydrogen bonding contacts [57–59]. Figure 8 demonstrates that the

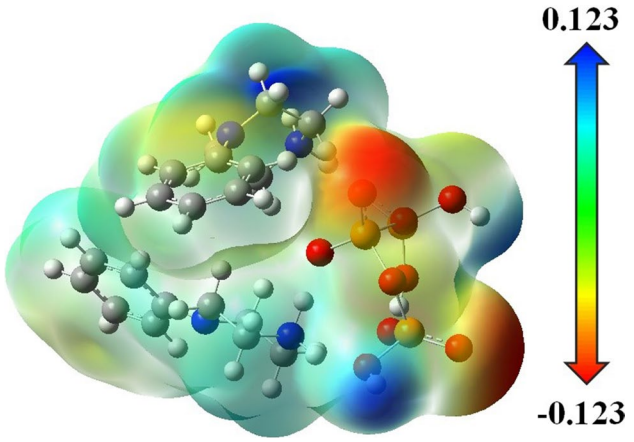

Fig. 8 The total electron density three-dimensional surface mapped for the compound with the electrostatic potential calculated at the B3LYP/LANL2DZ level

reactive sites are localized around the P-O group, and this region (deepest red) has the most negative potential spots over the oxygen atoms due to the C-H···O, N–H···O, and O–H···O interactions in the crystal structure. The negative potential value (−0.123 a.u.) displays the strongest repulsion. The most positive region for $(C_{10}H_{15}N_2)_2H_3P_3O_{10}$ is placed on the hydrogen atoms and shows the strongest attraction sites involving the 1-phenylpiperazinium moieties.

Mulliken population analysis

Mulliken population method was used to obtain the total atomic charge distributions and to describe the electronic structure, molecular dipole moment, charge transfer mechanism, and polarizability. The Mulliken charges for the molecule were performed with B3LYP/LanL2DZ level of theory in the gas phase. The atomic charges play a key role in the application of quantum mechanical simulations [60]. The charge distribution on atoms is important in explaining donor and acceptor pairs and gaining insight into the overall activity of the compound. Mulliken is highly effective in detecting nucleophilic or electrophilic attacks and regions sensitive to other molecular interactions. The corresponding Mulliken charges are tabulated in Table 5.

From the results, it is clear that all hydrogen atoms in the molecule have a positive charge. Also, all phosphorus atoms P1, P2, and P3 possess positive. It is worthy to mention that the oxygen atoms (O1, O3, O6, O7, and O10) displayed maximum negative charges. Because of these oxygen atoms' environment, all phosphorus atoms have higher Mulliken atomic charge than other positive atoms. The maximum of positive charges of carbon and nitrogen atoms were bonded to oxygen atoms. The results are supported with electrophilic/nucleophilic nature of MEP surface.

NMR spectroscopy

^{13}C NMR spectrum of the title compound is shown in Fig. S5a. Since the organic motif is symmetric and contains ten carbon atoms, each one has its own electronic environment. But as shown from the spectrum, it exhibits only six resonances. According to previous studies [61, 62], the carbons observed between 40 and 50 ppm are assigned to the nitrogen-bonded CH_2 groups while the aromatic carbons typically occur between 115 and 150 ppm. It is obvious that the peak at 149 ppm corresponds to the carbon bonded to the strongly attracting nitrogen atom. The ^1H NMR spectrum of the title compound is shown in Fig. S5b; a total often peaks were observed corresponding to fifteen hydrogens. The signals observed at 3.40 ppm and 3.41 ppm are assigned to C(8,10)H_2 and C(7,11)H_2 respectively. At 4.7 ppm, there is a simple signal which is normally the chemical shift of the water proton (as solvent). It is important to note that the range [6–7.5 ppm] is a common zone for aromatic ring protons. The triplet associated with the signals 7.05 ppm, 7.07 ppm, and 7.08 ppm is attributed to C(5)H. However, the ^1H signals of C(1)H and C(3)H appear at 7.11 ppm and 7.13 ppm. Finally, the C(6)H and C(4)H are indeed observed at 7.35 ppm, 7.37 ppm, and 7.39 ppm.

UV–vis absorption

The solid state UV–vis absorption spectrum of the entitled compound, measured at room temperature in the range 200–800 nm, is presented in Fig. S6. As can be seen, two distinct peaks with different intensities and wavelength are observed in the absorption spectrum. The intense peak around 294 nm can be ascribed to the π-π* transition of the aromatic ring of the phenyl group, whereas the weak band near 409 nm probably may originate from the n-π* transition of the triphosphoric anion. The determination of the optical band gap (E_g), which is a pivotal parameter for describing the solid state materials, can be evaluated based on the model proposed by Tauc [63] by plotting $(\alpha h\upsilon)^2$ versus $h\upsilon$ (α is the absorption coefficient and $h\upsilon$ is the energy of the incident photon where h represents the Planck's constant and υ is the frequency of vibration). The absorption edge is offered by the extrapolation of the curve until the energy axis. As shown in Fig. S7, the value of the optical band gap is 2.82 eV, which proves that the studied compound is a semiconductor and could be used for optical applications in far UV and optoelectronics [64]. The band gap between HOMO and LUMO calculated with DFT was found to be 3.27 eV which is very close in value to the optical band gap (2.82 eV).

Table 5 Main interatomic distances (Å) and bond angles (°) of $H_3P_3O_{10}^{2-}$

Atom	Mulliken charges	Atom	Mulliken charges	Atom	Mulliken charges
P1	1.595940	C8	0.125834	H7B	0.270348
P2	1.643224	C9	0.107889	H8	0.466642
P3	1.569168	C10	0.115469	H8A	0.229601
N1	−0.233178	C11	0.450929	H8B	0.294974
N2	0.377951	C12	−0.071320	H9	0.414848
N3	−0.230890	C13	0.012687	H9A	0.235052
N4	0.351232	C14	−0.023401	H9B	0.241049
O1	−0.893880	C15	0.012330	H10A	0.215997
O2	−0.285345	C16	−0.159340	H10B	0.253230
O3	−0.817813	C17	0.059153	H12	0.298006
O4	−0.836900	C18	0.187230	H13	0.242470
O5	−0.908279	C19	0.192000	H14	0.228287
O6	−0.706333	C20	0.057147	H15	0.221934
O7	−0.798426	H2	0.248241	H16	0.234190
O8	−0.288944	H2A	0.482747	H17A	0.241316
O9	−0.294988	H2B	0.363695	H17B	0.191109
O10	−0.655541	H3	0.225198	H18A	0.220024
C1	0.389041	H4	0.229381	H18B	0.339960
C2	−0.159094	H4A	0.496451	H19A	0.310768
C3	0.015923	H4B	0.330616	H19B	0.237912
C4	−0.015785	H5	0.241883	H20A	0.204472
C5	−0.007457	H6	0.343693	H20B	0.250085
C6	−0.036663	H7	0.415521		
C7	0.160428	H7A	0.228661		

Solid state photoluminescence property

Photoluminescence referred to as PL is a nondestructive method which is widely used to identify the luminescence property of the crystalline material. To further understand and study the optical properties of $(C_{10}H_{15}N_2)_2.H_3P_3O_{10}$, the photoluminescence was recorded in the solid state at room temperature over a spectral range from 360 to 470 nm and the spectrum is shown in Fig. S8. The emission spectrum at an excitation wavelength choosing at $\lambda_{ex} = 294$ nm presents one band of luminescence located around 351 nm. This luminescence originates from the intraligand π-π* of the transition of the 1-phenylpiperazinium cation. In order to determine fluorescence quantum yield of the title compound, pyrene (quantum yield $\phi_r = 0.32$ in cyclohexane) was used as a reference. The fluorescence quantum yield [65] can be calculated from the following equation [66]:

$$\phi_s = \phi_r \frac{I_s A_r \eta_s^2}{I_r A_s \eta_r^2}$$

where the subscripts s and r stand for sample and reference, respectively. ϕ_r denotes the fluorescence quantum yield of reference. I stand for the integrated area under the emission curves. A is the absorbance at a particular excitation wavelength. η is the refractive index of the medium. The absorbance of the dye at the excitation wavelength was always kept ~0.1. The fluorescence quantum yield of 1-phenylpiperazinium trihydrogen triphosphate using the relative method was determined to be 0.60. This value claims that the synthesized compound is significantly high luminescent.

Viability assays

As depicted in Fig. 9, experiments with cells were performed by measuring cell viability in the presence of a wide range of concentrations of $(C_{10}H_{15}N_2)_2H_3P_3O_{10}$ (from 10 nM to 100 µM) upon incubation for 24 h. Remarkably, no significant cytotoxic effect was observed even at high concentrations in the micro molar range and cell viability remained around 100% in all cases. These results point out that this hybrid material has no short-term cytotoxicity and is biocompatible under the conditions studied, which opens the possibility for its use in biological contexts.

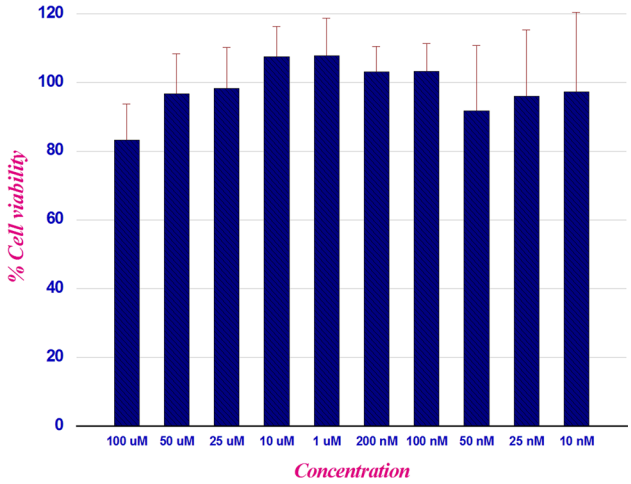

Fig. 9 Cell viability determined in RAW 264.7 mouse macrophages after $(C_{10}H_{15}N_2)_2H_3P_3O_{10}$ treatment at different concentrations for 24 h

Conclusion

In this work, we have successfully synthesized a novel organic triphosphate. This is noteworthy since such family remained limited in comparison with other condensed phosphates. Our discovery has been characterized by using different physicochemical techniques. The crystal structure can be described as quasi infinite layers of anions and between them are inserted the organic cations to be built, via a variety of interactions, a three-dimensional network. The Hirshfeld surface analysis reveals the percentage of intermolecular contacts of the obtained products. The geometrical parameters, collected within the framework of DFT calculations by using B3LYP methods with LANL2DZ basis set, are well correlated with the experimental results. Detailed IR studies were carried out; as can be seen, there is a good conformity between the experimental results and the theoretical ones. Moreover, NMR spectra were acquired and the results are in line with the crystallographic data. Finally, the performance of the new organic triphosphate compound in a cellular context was also tested. Remarkably, the compound was not toxic even at concentrations as high as 100 µM, which suggests its biocompatibility.

Overall, we hope these results could inspire future works in the development of organic phosphates and other hybrid compounds.

Abbreviations DFT: Density functional theory; ORTEP: Oak Ridge Thermal Ellipsoid Plot; ID: Distortion indices; HOMO: Highest occupied molecular orbital; LUMO: Lowest unoccupied molecular orbital; MEP: Molecular electrostatic potential

Supplementary Information The online version contains supplementary material available at https://doi.org/10.1007/s00894-022-05047-5.

Author contribution Y.O. synthesized the compound, discussed the results, and wrote the manuscript, S.K. and N.D. performed the DFT calculations, C.T.P helped in the cytotoxicity assays, A.L.L. carried out the NMR experiments, R.M.M. reviewed the manuscript, and W.S. supervised the work and corrected the manuscript.

Funding This work is supported by the Tunisian National Ministry of Higher Education and Scientific Research.

Data availability N/A.

Code availability N/A.

Declarations

Conflict of interest The authors declare no competing interests.

References

1. Rajkumar R, Praveen Kumar P (2019) Structure, crystal growth and characterization of piperazinium bis (4-nitrobenzoate) dihydrate crystal for nonlinear optics and optical limiting applications. J Mol Struct 1179:108–117. https://doi.org/10.1016/j.molstruc.2018.10.085
2. Chaouachi S, Hamdi B, Zouari R (2017) Crystal structure, electrical study and dielectric behavior of a new centrosymmetric hybrid material. Synth Met 223:122–213. https://doi.org/10.1016/j.synthmet.2016.11.030
3. Hamdi M, Karoui S, Oueslati A, Kamoun S, Hlel F (2018) Synthesis, crystal structure and dielectric properties of the new organic-inorganic hybrid compound $[C_6H_{10}N_2]_7[Bi_2Cl_{11}]2.4[Cl]$. J Mol Struct 1154:516–523. https://doi.org/10.1016/j.molstruc.2017.10.063
4. Karoui K, Rhaiem AB, Guidara K (2012) Dielectric properties and relaxation behavior of [TMA] 2Zn0. 5Cu0. $5Cl_4$ compound. Phys B407:489–493. https://doi.org/10.1016/j.physb.2011.11.021
5. Hachani A, Dridi I, Elleuch S, Roisnel T, Kefi R (2019) Crystal structure, spectroscopic and biological study of a new inorganic-organic hybrid compound $[Cd_4Cl_{12}(H_2O)_2]n$ $(C_{10}N_4H_{28})n$. Inorg Chem Commun 100:134–143. https://doi.org/10.1016/j.inoche.2018.12.006
6. Hajji R, Fersi MA, Hajji S, Hlel F, Ben Ahmed A (2019) Hirshfeld surface analysis, vibrational spectra, optical, DFT studies and biological activities of (C7H12N2)2[SnCl6]Cl2. 1.5H2O compound. Chem Phys Lett 722:160–172. https://doi.org/10.1016/j.cplett.2019.02.045
7. Kamminga ME, Gélvez-Rueda MC, Maheshwari S, van Droffelaar IS, Baas J, Blake GR, Grozema FC, Palstra TTM (2019) Electronic mobility and crystal structures of 2,5-dimethylanilinium triiodide and tin-based organic-inorganic hybrid compounds. J Solid State Chem 270:593–600. https://doi.org/10.1016/j.jssc.2018.12.029
8. Henchiri R, Ennaceur N, Cordier M, Ledoux-Rak I, Elaloui E (2017) Synthesis, X-ray crystal structure and highly non-linear optical properties of inorganic-organic hybrid compound: 1,4-diazbicyclo-octane oxonium tri- nitrates single crystal. J Phys Chem Solids 106:58–64. https://doi.org/10.1016/j.jpcs.2017.02.011
9. Oueslati Y, Kansız S, Valkonen A, Sahbani T, Dege N, Smirani W (2019) Synthesis, crystal structure, DFT calculations, Hirshfeld surface, vibrational and optical properties of a novel hybrid

non-centrosymmetric material $(C_{10}H_{15}N_2)_2H_2P_2O_7$. J Mol Struct 1196:499–507. https://doi.org/10.1016/j.molstruc.2019.06.110
10. Ben Rached A, Guionneau P, Lebraud E, Mhiri T, Elaoud Z (2017) Structural versus electrical properties of an organic-inorganic hybrid material based on sulfate. J Phys Chem Solids 100:25–32. https://doi.org/10.1016/j.jpcs.2016.09.006
11. Nenwa J, Djomo ED, Nfor EN, Djonwouo PL, Mbarki M, Fokwa BPT (2015) Two novel organic–inorganic hybrid compounds with straight and zigzag chain alignments of Cu(II) centers: synthesis, crystal structure, spectroscopy, thermal analysis and magnetism. Polyhedron 99:26–33. https://doi.org/10.1016/j.poly.2015.06.023
12. Vishwakarma AK, Kumari R, Ghalsasi PS, Arulsamy N (2017) Crystal structure, thermochromic and magnetic properties of organic-inorganic hybrid compound: $(C_7H_7N_2S)_2CuCl_4$. J Mol Struct 1141:93–98. https://doi.org/10.1016/j.molstruc.2017.03.076
13. Teiten M-H, Dicato M, Diederich M (2014) Hybrid curcumin compounds: a new strategy for cancer treatment. Molecules 19:20839–20863. https://doi.org/10.3390/molecules191220839
14. Ruiz-Hitzky E, Aranda P, Darder M, Rytwo G (2010) Hybrid materials based on clays for environmental and biomedical applications. J Mater Chem 20:9306–9321. https://doi.org/10.1039/C0JM00432D
15. Smirani W, Nasr CB, Rzaigui M (2004) Synthesis and crystal structure of a new o-ethylphenylammonium triphosphate $[2\text{-}C_2H_5C_6H_4NH_3]3H_2P_3O_{10}$. Mater Res Bull 39:1103–1111. https://doi.org/10.1016/j.materresbull.2004.02.013
16. Smirani W, Nasr CB, Rzaigui M (2004) Synthesis and structure characterization of piperazine1,4-diium triphosphate. Phosphorus Sulfur Silicon Relat Elem 179:2195–2204. https://doi.org/10.1080/10426500490475003
17. Sta W, Mohamed R (2005) Crystal structure of tris(3,5-diinethoxyanilinium) dihydrogentriphosphate, $[(CH_3O)_2(C_6H_3NH_3)]_3[H_2P_3O_{10}]$. Z Kristallogr NCS 220:250–252. https://doi.org/10.1524/ncrs.2005.220.14.260
18. Sta W, Mohamed R (2005) Structural characterization of a new organic triphosphate, $[4\text{-}(OCH_3)C_6H_4CH_2NH_3]_4H_2P_3O_{10}H_4P_3O_{10}$. Anal Sci: X-Ray Struct Anal Online 21:x109–x110. https://doi.org/10.2116/analscix.21.x109
19. Smirani W (2007) Crystal structure and spectroscopic studies of $[2,6\text{-}(C_2H_5)_2C_6H_3NH_3]_2H_3P_3O_{10}$. Phosphorus Sulfur Silicon Relat Elem 182:1727–1737. https://doi.org/10.1080/10426500701313904
20. Souissi S, Smirani W, Nasr CB, Rzaigui M (2007) Structural and physicochemical studies of $[2,3\text{-}(CH_3)_2C_6H_3NH_3]_4HP_3O_{10}.2H_2O$. Phosphorus Sulfur Silicon Relat Elem 182:2731–2743. https://doi.org/10.1080/10426500701519336
21. Mechergui J, Belam W, Mohamed R (2007) Crystal structure of 1-(2,3-dimethylphenyl) piperazinium dihydrogentriphosphate trihydrate, $[C_{12}H_{19}N2]_3[H_2P_3O_{10}]$. $3H_2O$. Z Kristallogr NCS 222:409–411. https://doi.org/10.1524/ncrs.2007.0174
22. Belghith S, Hamada LB, Jouini A (2013) Crystal structure and physicochemical properties of a new 4,4′-diammoniumdiphenylether triphosphate [C12H14N2O]2HP3O10.2H2O. J Inorg Organomet Polym Mater 23:779–783. https://doi.org/10.1007/s10904-013-9831-z
23. Ryckebusch A, Debreu-Fontaine M-A, Mouray E, Grellier P, Sergheraert C, Melnyk P (2005) Synthesis and antimalarial evaluation of new N1-(7-chloro-4-quinolyl)-1,4-bis(3-aminopropyl)piperazine derivatives. Bioorg Med Chem Lett 15:297–302. https://doi.org/10.1016/j.bmcl.2004.10.080
24. Ryckebusch A, Deprez-Poulain R, Debreu-Fontaine M-A, Vandaele R, Mouray E, Grellier P, Sergheraert C (2003) Synthesis and antimalarial evaluation of new 1,4-bis(3-aminopropyl)piperazine derivatives. Bioorg Med Chem Lett 13:3783–3787. https://doi.org/10.1016/j.bmcl.2003.07.008
25. Wang S-F, Yin Y, Qiao F, Wu X, Sha S, Zhang L, Zhu H-L (2014) Synthesis, molecular docking and biological evaluation of coumarin derivatives containing piperazine skeleton as potential antibacterial agents. Bioorg Med Chem 22:2409–2415. https://doi.org/10.1016/j.bmc.2014.09.048
26. Yevich JP, New JS, Smith DW, Lobeck WG, Catt JD, Minielli JL, Eison MS, Taylor DP, Riblet LA, Temple DL (1986) Synthesis and biological evaluation of 1-(1,2-benzisothiazol-3-yl) and (1,2-benzisoxazol-3-yl) piperazine derivatives as potential antipsychotic agents. J Med Chem 29:359–369. https://doi.org/10.1021/jm00153a010
27. Bhosale SH, Kanhed AM, Dash RC, Suryawanshi MR, Mahadik KR (2014) Design, synthesis, pharmacological evaluation and computational studies of 1-(biphenyl-4-yl)-2-[4-(substituted phenyl)-piperazin-1-yl]ethanones as potential antipsychotics. Eur J Med Chem 74:358–365. https://doi.org/10.1016/j.ejmech.2013.12.043
28. Bali A, Malhotra S, Dhir H, Kumar A, Sharma A (2009) Synthesis and evaluation of 1-(quinoliloxypropyl)-4-aryl piperazines for atypical antipsychotic effect. Bioorg Med Chem Lett 19:3041–3044. https://doi.org/10.1016/j.bmcl.2009.04.019
29 Suryavanshi H, Rathore M (2017) Synthesis and biological activities of piperazine derivatives as antimicrobial and antifungal agents. Org Commun 10:228–238. https://doi.org/10.25135/acg.oc.23.17.05.026
30. Koparde S, Hosamani KM, Kulkarni V, Joshi SD (2018) Synthesis of coumarin-piperazine derivatives as potent anti-microbial and anti-inflammatory agents, and molecular docking studies. Chem Data Collect 15–16:197–206. https://doi.org/10.1016/j.cdc.2018.06.001
31. Sheldrick G (2015) *SHELXT* -integrated space-group and crystal-structure determination. Acta Cryst A71:3–8. https://doi.org/10.1107/S2053273314026370
32. Sheldrick GM (2015) Crystal structure refinement with SHELXL. Acta Cryst C71:3–8. https://doi.org/10.1107/S2053229614024218
33. Brandenburg K (1998) DIAMOND Version 2.0
34. Wolff S, Grimwood D, McKinnon J, Turner M, Jayatilaka D, Spackman M (2012) Crystal explorer. The University of Western Australia Perth, Australia
35. Frisch MJ, Trucks GW, Schlegel HB, Scuseria GE, Robb MA, Cheeseman JR, Montgomery JA Jr, Vreven T, Kudin KN, Burant JC, Millam JM, Iyengar SS, Tomasi J, Barone V, Mennucci B, Cossi M, Scalmani G, Rega N, Petersson GA, Nakatsuji H, Hada M, Ehara M, Toyota K, Fukuda R, Hasegawa J, Ishida M, Nakajima T, Honda Y, Kitao O, Nakai H, Klene M, Li X, Knox JE, Hratchian HP, Cross JB, Bakken V, Adamo C, Jaramillo J, Gomperts R, Stratmann RE, Yazyev O, Austin AJ, Cammi R, Pomelli C, Ochterski JW, Ayala PY, Morokuma K, Voth GA, Salvador P, Dannenberg JJ, Zakrzewski VG, Dapprich S, Daniels AD, Strain MC, Farkas O, Malick DK, Rabuck AD, Raghavachari K, Foresman JB, Ortiz JV, Cui Q, Baboul AG, Clifford S, Cioslowski J, Stefanov BB, Liu G, Liashenko A, Piskorz P, Komaromi I, Martin RL, Fox DJ, Keith T, Al- Laham MA, Peng CY, Nanayakkara A, Challacombe M, Gill PMW, Johnson B, Chen W, Wong MW, Gonzalez C, Pople JA (2004) Gaussian 03, Revision E.01. Gaussian, Inc., Wallingford
36. Dennington R II, Keith T, Millam J (2007) Gauss View, Version 4.1.2. Semichem Inc., Shawnee Mission
37. Tamer Ö, Avcı D, Atalay Y (2016) Synthesis, X-ray crystal structure, photophysical characterization and nonlinear optical properties of the unique manganese complex with picolinate and 1,10 phenantroline: toward the designing of new high NLO response crystal. J Phys Chem Solids 99:124–133. https://doi.org/10.1016/j.jpcs.2016.08.013

38. Baur W (1974) The geometry of polyhedral distortions. Predictive relationships for the phosphate group. Acta Cryst B30:1195–1215. https://doi.org/10.1107/S0567740874004560
39. Cremer D, Pople JA (1975) General definition of ring puckering coordinates. J Am Chem Soc 97:1354–1358. https://doi.org/10.1021/ja00839a011
40. Hansia P, Guruprasad N, Vishveshwara S (2006) Ab initio studies on the tri- and diphosphate fragments of adenosine triphosphate. Biophys Chem 119:127–136. https://doi.org/10.1016/j.bpc.2005.07.011
41. McKinnon JJ, Spackman MA, Mitchell AS (2004) Novel tools for visualizing and exploring intermolecular interactions in molecular crystals. Acta Cryst B60:627–668. https://doi.org/10.1107/S0108768104020300
42. Spackman MA, Jayatilaka D (2009) Hirshfeld surface analysis. Cryst Eng Comm 11:19–32. https://doi.org/10.1039/B818330A
43. Spackman MA, Byrom PG (1997) A novel definition of a molecule in a crystal. Chem Phys Lett 267:215–220. https://doi.org/10.1016/S0009-2614(97)00100-0
44. Ilmi R, Kansız S, Dege N, Khan MS (2019) Synthesis, structure, Hirshfeld surface analysis and photophysical studies of red emitting europium acetylacetonate complex incorporating a phenanthroline derivative. J Photochem Photobiol A 377:268–281. https://doi.org/10.1016/j.jphotochem.2019.03.036
45. Kansiz S, Dege N, Topcu Y, Atalay Y, Gaidai SV (2018) Crystal structure and Hirshfeld surface analysis of (succinato κO)[N, N, N′, N′ tetrakis(2 hydroxyethyl)ethylenediamine κ5O, N, N′, O′, O″]nickel(II) tetrahydrate. Acta Crystallogr E74:1700–1704. https://doi.org/10.1107/S2056989018015359
46. Kansız S, Tolan A, İçbudak H, Dege N (2019) Synthesis, crystallographic structure, theoretical calculations, spectral and thermal properties of trans-diaquabis(trans-4-aminoantipyrine)cobalt(II) acesulfamate. J Mol Struct 1190:102–115. https://doi.org/10.1016/j.molstruc.2019.04.058
47. Guerrab W, Chung I-M, Kansiz S, Mague JT, Dege N, Taoufik J, Salghi R, Ali IH, Khan MI, Lgaz H, Ramli Y (2019) Synthesis, structural and molecular characterization of 2,2-diphenyl-2H,3H,5H,6H,7H-imidazo[2,1-b][1,3]thiazin-3-one. J Mol Struct 1197:369–376. https://doi.org/10.1016/j.molstruc.2019.07.081
48. Gabelica-Robert M, Tarte P (1982) Infrared spectrum of crystalline and glassy pyrophosphates: preservation of the pyrophosphate group in the glassy structure. J Mol Struct 79:251–254. https://doi.org/10.1016/0022-2860(82)85061-8
49. Cornilson BC (1984) Solid state vibrational spectra of calcium pyrophosphate dihydrate. J Mol Struct 117:1–9. https://doi.org/10.1016/0022-2860(84)87237-3
50. Sivakumar C, Balachandran V, Narayana B, Salian VV, Revathi B, Shanmugapriya N, Vanasundari K (2021) Molecular spectroscopic investigation, quantum chemical, molecular docking and biological evaluation of 2-(4-Chlorophenyl)-1-[3-(4-chlorophenyl)-5-[4-(propan-2-yl) phenyl-3, 5-dihydro-1H-pyrazole-yl] ethanone. J Mol Struct 1224:129010. https://doi.org/10.1016/j.molstruc.2020.129010
51. Shoba D, Karabacak M, Periandy S, Ramalingam S (2011) FT-IR and FT-Raman vibrational analysis, ab initio HF and DFT simulations of isocyanic acid 1-naphthyl ester. Spectrochim Acta Part A 81:504–518. https://doi.org/10.1016/j.saa.2011.06.044
52. Kansız S, Dege N (2018) Synthesis, crystallographic structure, DFT calculations and Hirshfeld surface analysis of a fumarate bridged Co(II) coordination polymer. J Mol Struct 1173:42–51. https://doi.org/10.1016/j.molstruc.2018.06.071
53. Ersanli CC, Kantar GK, Şaşmaz S (2017) Crystallographic, spectroscopic (FTIR and NMR) and quantum computational calculation studies on bis(2-methoxy-4-((*E*)-prop-1-enyl)phenyl) oxalate. J Mol Struct 1143:318–327. https://doi.org/10.1016/j.molstruc.2017.04.032
54. Tankov I, Yankova R (2019) Hirshfeld surface, DFT vibrational (FT-IR) and electronic (UV–vis) studies on 4-amino-1H-1,2,4-triazolium nitrate. J Mol Struct 1179:581–592. https://doi.org/10.1016/j.molstruc.2018.11.050
55. Pearson RG (1988) Absolute electronegativity and hardness: application to inorganic chemistry. Inorg Chem 27:734–740. https://doi.org/10.1021/ic00277a030
56. Sastri V, Perumareddi J (1997) Molecular orbital theoretical studies of some organic corrosion inhibitors. Corrosion 53:617–622. https://doi.org/10.5006/1.3290294
57. Şen F, Kansiz S, Uçar I (2017) A one-dimensional copper(II) coordination polymer incorporating succinate and N, N-diethylethylenediamine ligands: crystallographic analysis, vibrational and surface features, and DFT analysis. Acta Crystallogr C 73:517–524. https://doi.org/10.1107/S2053229617008452
58. Demircioğlu Z, Ersanli CC, Kantar GK, Şaşmaz S (2019) Spectroscopic, Hirshfeld surface, X-ray diffraction methodologies and local & global chemical activity calculations of 5-(2-methoxy-4-(prop-1-en-1-yl)phenoxy)pyrazine-2,3-dicarbonitrile. J Mol Struct 1181:25–37. https://doi.org/10.1016/j.molstruc.2018.12.072
59. Tankov I, Yankova R (2019) Mechanistic investigation of molecular geometry, intermolecular interactions and spectroscopic properties of pyridinium nitrate. Spectrochim Acta A 219:53–67. https://doi.org/10.1016/j.saa.2019.04.027
60. Gopi V, Subbiahraj S, Chemmanghattu K, Ramamurthy PC (2020) 2,3-di(2-furyl) quinoxaline bearing 3 -ethyl rhodanine and 1,3 indandione based heteroaromatic conjugated T-shaped push-pull chromophores: design, synthesis, photophysical and non-linear optical investigations. Dyes Pigments 173:107887. https://doi.org/10.1016/j.dyepig.2019.107887
61. Khedhiri L, Hamdi A, Soudani S, Kaminsky W, Lefebvre F, Jelsch C, Wojtaś M, Ben Nasr C (2018) Crystal structure, Hirshfeld surface analysis, thermal behavior and spectroscopic investigations of a new organic cyclohexaphosphate, $(C_{10}H_{15}N_2)_4(Li)_2(P_6O_{18})(H_2O)_6$. J Mol Struct 1171:429–437. https://doi.org/10.1016/j.molstruc.2018.06.015
62. Essid M, Aloui Z (2019) Synthesis, Hirshfeld surface analysis and physicochemical studies of non-centrosymmetric semi-organic compound: $[C_{10}H_{15}N_2](H_2PO_4)$. Chem Data Collect 24:100285. https://doi.org/10.1016/j.cdc.2019.100285
63. Tauc J (1968) Optical properties and electronic structure of amorphous Ge and Si. Mater Res Bull 3:37–46. https://doi.org/10.1016/0025-5408(68)90023-8
64. Franklin S, Balasubramanian T, Nehru K, Kim Y (2009) Crystal structure, conformation, vibration and optical band gap analysis of bis [rac-propranolol nitrate]. J Mol Struct 927:121–125. https://doi.org/10.1016/j.molstruc.2009.03.003
65. Lagorio MG (2020) Determination of fluorescence quantum yields in scattering media. Methods Appl Fluoresc 8:043001. https://doi.org/10.1088/2050-6120/aba69c
66. Würth C, Grabolle M, Pauli J, Spieles M (2013) Relative and absolute determination of fluorescence quantum yields of transparent samples. U Resch-Genger Nat Protoc 8:1535–1550. https://doi.org/10.1038/nprot.2013.087